Nuclear Theory'22
ed. V. Nikolaev, Heron Press, Sofia, 2003

Microscopic Studies in Neutron-Rich Matter

F. Sammarruca

Physics Department, University of Idaho, Moscow, ID 83844, U.S.A

Abstract.

Microscopic calculations of nuclear matter properties with unequal densities of protons and neutrons are discussed. We employ realistic two-body forces and the Dirac-Brueckner-Hartree-Fock approach. Results are compared with recent experimental constraints on the high-density behaviour of the equation of state. Predictions for energies, proton and neutron r.m.s. radii, and neutron skins of some closed-shell nuclei are also presented. These are based upon our equation of state for asymmetric matter which is used as input for an energy functional. We compare with experimental information, when available, and point out the need for accurate determinations of neutron densities and skins.

1 Introduction

One of the main challenges in nuclear physics is to understand how the properties of nuclei arise from the interactions among the protons and the neutrons. The ability to vary the ratio between protons and neutrons over a large range is a crucial tool to reach that understanding, but has so far been rather limited. The advent of beams of short-lived, radioactive nuclei promises to change this situation, providing new opportunities to explore unknown regions and possibly phenomena and symmetries different than those seen in the stability region. If approved for construction, the Rare Isotope Accelerator (RIA) will allow the study of unique nuclear systems which are expected to exist at the boundaries of the nuclear chart.

Furthermore, studies of the strong interactions between protons and neutrons in exotic matter are important for our understanding of astrophysical processes, such as structure of neutron stars and what supports them against gravitational collapse. Thus, it is important and timely to develop microscopic effective interactions which can account for the asymmetry between proton and neutron densities.

Neutron skins are crucial observables and may have impact on phenomena such as phase transitions inside a neutron star. Recent calculations by Horowitz and Piekarewicz [1] have suggested a relation between the skin of a heavy nucleus and the properties of neutron star crusts. A softer symmetry energy implies larger central densities and thus smaller radii. However, although a strong correlation is found between skin thickness and star radius, the latter is not uniquely constrained by a measurement of the neutron skin, because the skin depends on the nuclear matter equation of state (EOS) at or below saturation density, while the star radius is also sensitive to the high density behaviour of the EOS. Separate measurements of the two could provide valuable information on the EOS at low and high densities [1].

Our knowledge of matter distribution inside asymmetric nuclei must be improved and broadened. The doubly magic nucleus ^{208}Pb is perhaps one of the most asymmetric nuclei for which a considerable database exists. Nevertheless, determinations of neutron densities differ considerably depending on the model used in the analysis [2], while almost nothing is known about much more neutron-rich nuclei. The recent analysis by Clark, Kerr, and Hama [3] finds values of neutron r.m.s. radii and neutron skins generally not in agreement with those predicted by relativistic mean-field models, which are typically larger. In Ref. [4], Furnstahl investigates the spread in neutron skin predictions for ^{208}Pb within mean-field models. The nature of that variation is studied using correlations between basic properties of the models and neutron skin thickness in ^{208}Pb. The results suggest that mean-field models may overestimate the skin thickness and that additional constraints may be needed to improve the model functionals [4].

Phenomenological EOS based on the non-relativistic Skyrme Hartee-Fock theory and the relativistic mean field theory, respectively, have been used to predict neutron skins of Na isotopes [5]. When compared with the available data [6], which carry considerable uncertainties, the two calculations appear to be the two extreme cases bounding a region consistent with experiment. In summary, accurate measurements of neutron skins are needed to constrain theoretical models.

In this paper, first we describe our microscopic calculations of the EOS for asymmetric matter (Section 2). We use realistic nucleon-nucleon (NN) forces and the Dirac-Brueckner-Hartree-Fock (DBHF) framework. (More details can be found in Ref. [7].) We also calculate properties of astrophysical significance, such as the pressure in symmetric matter and neutron matter up to about five times saturation density, and compare with recent experimental constraints obtained from analyses of nuclear collisions [8]. In Section 3, we exploit the previously calculated EOS to make predictions for energies, proton and neutron radii, and neutron skins of finite nuclei based upon the EOS. We will use a liquid droplet model, which, in spite of its simplicity, provides a useful mean to relate the EOS directly to structural properties of nuclei, thus allowing a study of the

sensitivity of those properties to the EOS model. Our conclusions and future plans are summarized in Section 4.

2 Calculation of Asymmetric Matter Properties

By definition, nuclear matter is an idealized infinite system of protons and neutrons under their mutual strong interactions and without electromagnetic forces. When proton and neutron densities (ρ_p and ρ_n) are different, we speak of *asymmetric* nuclear matter.

It is also convenient to define the total density $\rho = \rho_n + \rho_p$ and the asymmetry (or neutron excess) parameter $\alpha = \dfrac{\rho_n - \rho_p}{\rho}$. Clearly, α=0 corresponds to symmetric matter, and α=1 to neutron matter.

In terms of α and the average Fermi momentum, related to the total density in the usual way,

$$\rho = \frac{2k_F^3}{3\pi^2}, \tag{1}$$

the neutron and proton Fermi momenta can be expressed as

$$k_F^n = k_F(1+\alpha)^{1/3} \tag{2}$$

and

$$k_F^p = k_F(1-\alpha)^{1/3}, \tag{3}$$

respectively.

We use the Thompson relativistic three-dimensional reduction of the Bethe-Salpeter equation. The Thompson equation is applied to nuclear matter in strict analogy to free-space scattering and reads, in the nuclear matter rest frame,

$$g_{ij}(\vec{q}',\vec{q},\vec{P},(\epsilon^*_{ij})_0) = v^*_{ij}(\vec{q}',\vec{q}) + \int \frac{d^3K}{(2\pi)^3} v^*_{ij}(\vec{q}',\vec{K}) \frac{m_i^* m_j^*}{E_i^* E_j^*} \frac{Q_{ij}(\vec{K},\vec{P})}{(\epsilon^*_{ij})_0 - \epsilon^*_{ij}(\vec{P},\vec{K})} g_{ij}(\vec{K},\vec{q},\vec{P},(\epsilon^*_{ij})_0) \tag{4}$$

where ij=nn, pp, or np, and the asterix signifies that medium effects are applied to those quantities. In Eq. (4), $\vec{q}$, $\vec{q}'$, and $\vec{K}$ are the initial, final, and intermediate relative momenta, and $E_i^* = \sqrt{(m_i^*)^2 + K^2}$. The momenta of the two interacting particles in the nuclear matter rest frame have been expressed in terms of their relative momentum and the center-of-mass momentum, $\vec{P}$, through

$$\vec{P} = \frac{\vec{k}_1 + \vec{k}_2}{2} \tag{5}$$

$$\vec{K} = \frac{\vec{k}_1 - \vec{k}_2}{2} \tag{6}$$

The energy of the two-particle system is

$$\epsilon^*_{ij}(\vec{P},\vec{K}) = e^*_i(\vec{P},\vec{K}) + e^*_j(\vec{P},\vec{K}) \tag{7}$$

and $(\epsilon^*_{ij})_0$ is the starting energy. The single-particle energy e^*_i includes kinetic energy and potential energy, see below. The Pauli operator, Q, prevents scattering to occupied states. To eliminate the angular dependence from the kernel of Eq. (4), it is customary to replace the exact Pauli operator with its angle-average. It is also customary to introduce an average center-of-mass momentum [9]. Detailed expressions for the case of two different Fermi momenta can be found in Ref. [7].

The goal is to determine self-consistently the nuclear matter single-particle potential which, in our case, will be different for neutrons and protons. To facilitate the description of the numerical procedure, we will use a schematic notation for the neutron/proton potential. We write, for neutrons,

$$U_n = U_{np} + U_{nn} \tag{8}$$

and for protons

$$U_p = U_{pn} + U_{pp} \tag{9}$$

where each of the four pieces on the right-hand-side of Eqs. (8-9) depends on the appropriate g-matrix (nn, pp, or np) from Eq. (4). Clearly, the two equations above are coupled through the np/pn components and so they must be solved simultaneously. Furthermore, the g-matrix equation and Eqs. (8-9) are coupled through the single-particle energy (which includes the single-particle potential). So we have three coupled equations to be solved self-consistently. As done in the symmetric case [10], we parametrize the single particle potential for protons and neutrons (Eqs. (8-9)) in terms of two constants, $U_{S,i}$ and $U_{V,i}$, (the scalar and vector potential) through

$$U_i(k_i) = \frac{m^*_i}{E^*_i} U_{S,i} + U_{V,i}. \tag{10}$$

where m^*_i is the effective mass, defined as

$$m^*_i = m_i + U_{S,i} \tag{11}$$

The subscript "i" signifies that these parameters are different for protons and neutrons. Starting from some initial values of $U_{S,i}$ and $U_{V,i}$, the g-matrix equation is solved and a first approximation for $U_i(k_i)$ is then obtained. This solution is again parametrized in terms of a new set of constants, and the procedure is repeated until convergence is reached. The effective masses for neutrons and protons, m^*_i, obtained through this procedure are shown in Figure 1 as a function of the Fermi momentum at various levels of asymmetry.

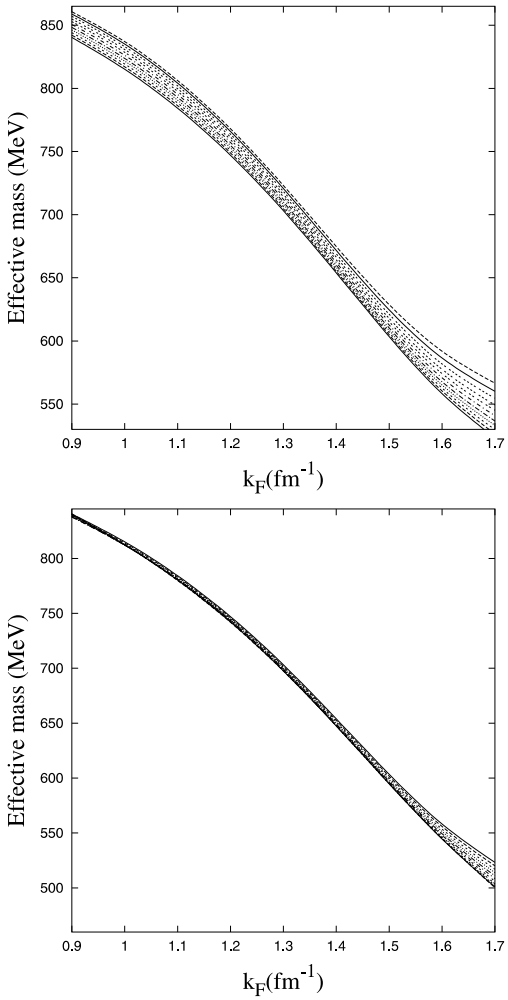

Figure 1. Upper panel: neutron effective mass as a function of the Fermi momentum and for increasing values of α between 0 and 1. The upper curve corresponds to $\alpha = 1$. Lower panel: proton effective mass. The upper curve corresponds to $\alpha = 0$.

Finally, the energy per neutron or proton in nuclear matter is calculated from

$$\bar{e}_i = < T_i > + < U_i > . \tag{12}$$

The EOS, or energy per nucleon as a function of density, is then written as

$$\bar{e}(\rho_n, \rho_p) = \frac{\rho_n \bar{e}_n + \rho_p \bar{e}_p}{\rho} \tag{13}$$

or

$$\bar{e}(k_F,\alpha) = \frac{(1+\alpha)\bar{e}_n + (1-\alpha)\bar{e}_p}{2}. \tag{14}$$

The NN potential used in this work is the relativistic OBEP from Ref. [11], which uses the Thompson equation and the pseudo-vector coupling for the π and η mesons.

The EOS as obtained from our DBHF calculation is displayed in Figure 2 (upper panel), as a function of k_F and for values of α between 0 and 1. The symmetric matter EOS saturates at $k_F \approx 1.4$ fm^{-1} with a value of 16.7 MeV, in good agreement with the empirical values. For the compression modulus of saturated symmetric matter, defined as

$$\kappa = k_F^2 \frac{\partial^2 \bar{e}(k_F)}{\partial^2 k_F}|_{k_F=k_F^{(0)}} \tag{15}$$

we find a value of 233 MeV. This is in excellent agreement with the recent empirical determination of 225$\pm$15 MeV [12].

With increasing neutron density (the total density remaining constant), the EOS becomes increasingly repulsive and the minimum shifts towards lower densities. As the system moves towards neutron matter, the "energy well" gets more and more shallow, until, for α larger than about 0.8, the system is no longer bound.

We also show for comparison the EOS based on the conventional Brueckner-Hartree-Fock (BHF) approach, see Figure 2, lower panel. Also in this case we have performed a self-consistent calculation based on the same realistic force. However, no medium modifications are included in the potential to account for the proper Dirac structure of the nucleons in nuclear matter. As a consequence of that, saturation of symmetric matter is obtained at a much higher density, a well-known problem with the conventional approach.

In Figure 3, we take a different look at the EOS. There, we plot the quantity $\bar{e}(k_F,\alpha) - \bar{e}(k_F,0)$ versus α^2. Clearly, the behaviour is linear, that is

$$\bar{e}(k_F,\alpha) - \bar{e}(k_F,0) = e_s\alpha^2, \tag{16}$$

or parabolic versus α. This linear behaviour, shared with the non-relativistic predictions, see lower panel of Figure 3, is reminiscent of the asymmetry term in the familiar semi-empirical mass formula. By reading the slope of each line, we can then predict the nuclear symmetry energy, defined as

$$e_s = \frac{1}{2}\frac{\partial^2 \bar{e}(k_F,\alpha)}{\partial^2 \alpha}|_{\alpha=0}. \tag{17}$$

This is shown in Figure 4, where the solid curve is the prediction from the DBHF model and the dashed corresponds to the BHF calculation. The DBHF prediction

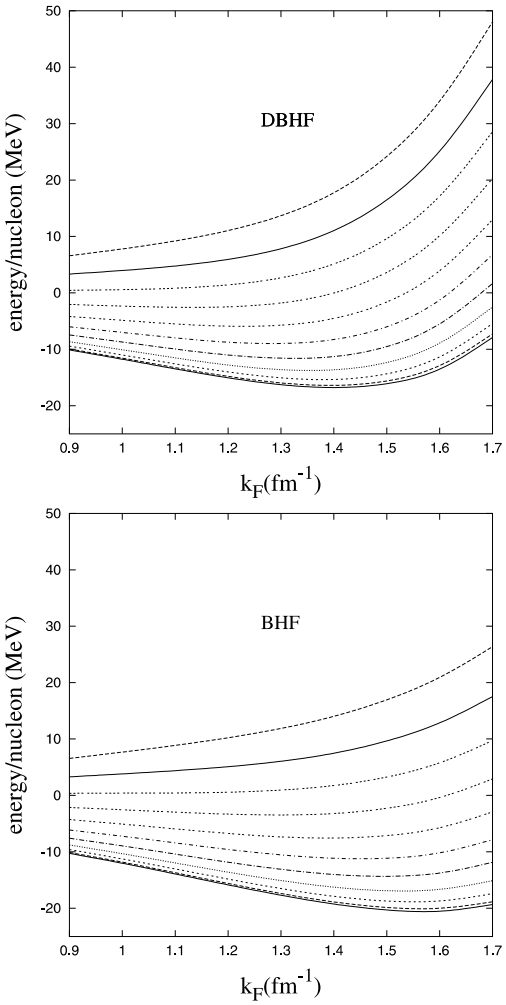

Figure 2. Upper panel: energy per nucleon as a function of the Fermi momentum at different values of the asymmetry parameter (in steps of 0.1) from symmetric matter (lowest curve) to neutron matter (highest curve). The predictions are obtained from DBHF calculations. Lower panel: corresponding predictions from BHF calculations.

at saturation density is about 30 MeV. The behaviour of the symmetry energy is most controversial at high densities, where even the trend depends strongly on the type of interaction used [13]. Energetic reactions induced by heavy neutron-rich nuclei have been proposed as a mean to obtain crucial information on the high-density behaviour of the nuclear symmetry energy and thus the EOS of

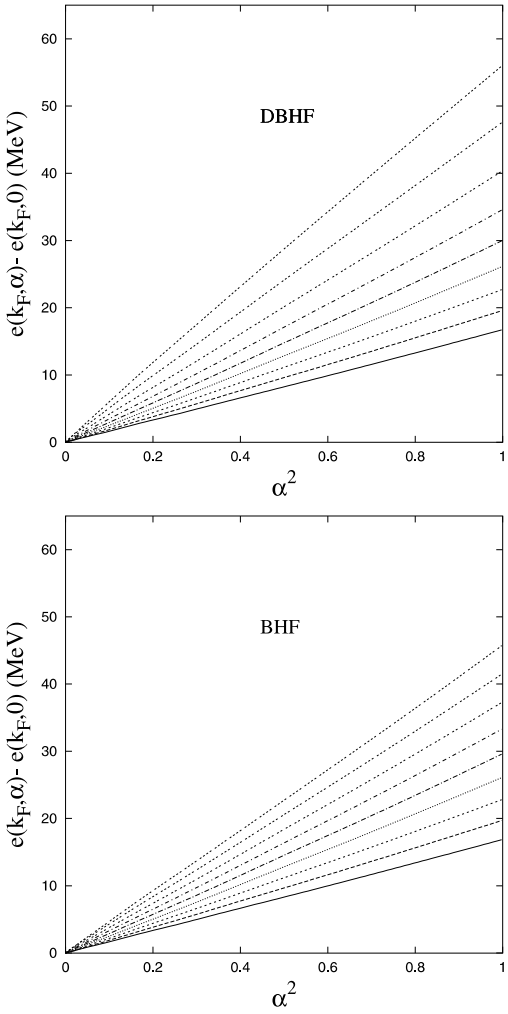

Figure 3. Upper panel: the left-hand side of Eq. (16) versus α^2 (DBHF model) for increasing values of the Fermi momentum from 0.9 fm^{-1} (lowest curve) to 1.7 fm^{-1}. Lower panel: corresponding predictions from BHF calculations.

dense neutron-rich matter [13]. Analyses of collision dynamics have been done at the National Superconducting Cyclotron Laboratory to extract EOS-sensitive observables such as the elliptic flow [8]. In this way, empirical constraint has been obtained for the pressure of symmetric and neutron matter at densities up to five times saturation density.

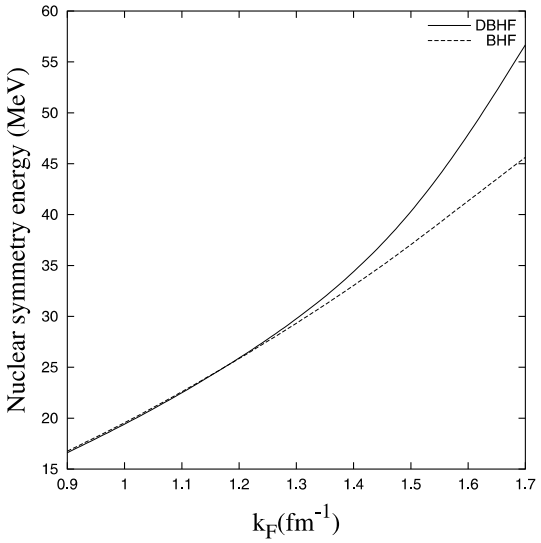

Figure 4. Nuclear symmetry energy as a function of the Fermi momentum. The solid line is the prediction from DBHF calculations, while the dashed line is obtained with the conventional Brueckner approach.

The pressure of neutron-rich matter is defined in terms of the energy/particle as

$$P(\rho,\alpha) = \rho^2 \frac{\partial \bar{e}(\rho,\alpha)}{\partial \rho} \tag{18}$$

In Figure 5, we show the pressure obtained from the DBHF-based EOS for symmetric matter and neutron matter. The empirical constraints have been provided by the authors of Ref. [8]. The area within the dashed lines indicates EOS consistent with the elliptic flow measurements reported in that work. For the case of neutron matter, two different parametrizations for the symmetry energy are assumed in the analysis. The two pressure contours in the bottom panel of Figure 5 correspond to the weakest (lower contour) and the strongest (higher contour) density dependence for $e_s(\rho)$ proposed by Prakash *et al.* [14].

It is fair to say that DBHF predictions produce a reasonable amount of repulsion. In contrast, relativistic mean field theories (RMFT) tend to generate too much pressure [8], as can be expected from the higher compression modulus usually predicted by those models. While very repulsive EOS such as obtained from RMFT as well as weakly repulsive EOS (compression modulus of 167 MeV) are ruled out by the analysis, EOS which become softer at densities higher than three times saturation density (possibly due to a phase transition to quark matter), are not excluded.

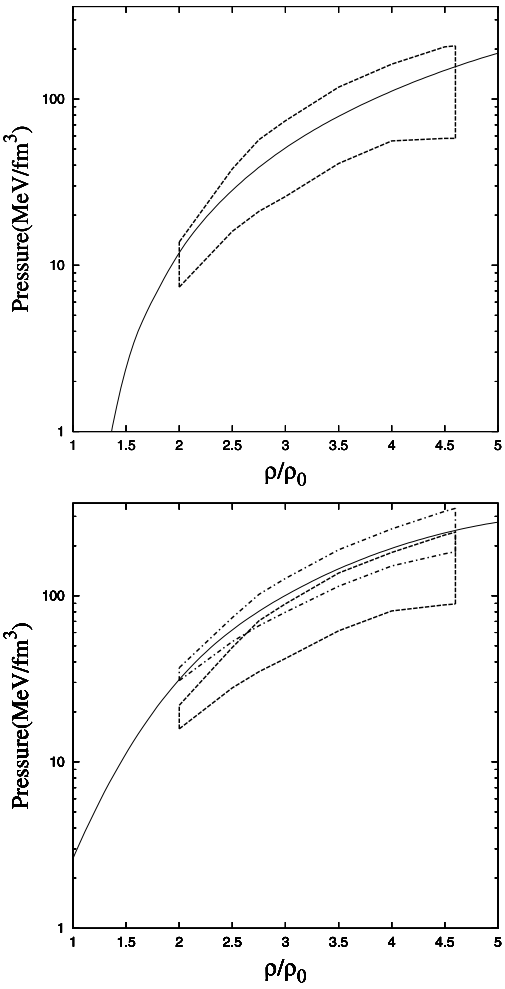

Figure 5. Upper panel: pressure (in MeV/fm^3) in symmetric matter as a function of density (in units of saturation density). The area within the dashed lines indicates pressure values consistent with the data. Lower panel: pressure in neutron matter. The two contours correspond to two parametrizations of the asymmetry term used in the analysis, as explained in the text. The predictions are from DBHF calculations.

3 EOS-based Predictions of Nuclear Energies and Radii

3.1 Description of the Model

A relatively straightforward way to relate the microscopic EOS directly to structural properties of finite nuclei is a liquid droplet model [5], where the "volume"

term is directly related to the EOS. Schematically, one may write the energy of a nucleus in terms of an energy functional,

$$E = \int_0^\infty \bar{e}(\rho_n(r), \rho_p(r))\rho(r)4\pi r^2 dr + \int_0^\infty f_0 |\bigtriangledown \rho(r)|^2 4\pi r^2 dr + \frac{e^2}{4\pi\epsilon_0}(4\pi)^2 \int_0^\infty dr' r' \rho_p(r') \int_0^{r'} dr \rho_p(r) r^2 \quad (19)$$

where the last two terms on the right-hand side are the surface energy and the Coulomb energy, respectively. The latter is calculated integrating the electrostatic interaction between a uniformly charged sphere of radius r' and a uniformly charged spherical shell of thickness dr'. The constant f_0 is taken to be 70 MeVfm^5 from fits to binding energies and radii of β-stable nuclei [15]. The integrand in the first term contains precisely the EOS for asymmetric matter. The proton and neutron densities, or, equivalently, the total density $\rho(r)$=$\rho_n(r) + \rho_p(r)$ and the neutron excess parameter $\alpha(r)$ =$(\rho_n(r) - \rho_p(r))/\rho(r)$, are now functions of the radial coordinate.

One can then parametrize the proton and neutron density functions and search for the values of those parameters that maximize the binding energy of the nucleus. For this test calculation, we have used standard two-parameter Fermi distributions, that is

$$\rho_i(r) = \frac{a_i}{1 + e^{(r-b_i)/c_i}} \quad (20)$$

with $i = n, p$ for neutron/proton, respectively. The parameters b_i and c_i are the radius and diffuseness, and the value of a_i is determined by normalizing the density distributions to N or Z. For each set of trial parameters, the functions $\rho(r)$ and $\alpha(r)$ are evaluated over the integration range, and the the EOS is interpolated as a function of two variables. Alternatively, we can save one interpolation by writing the EOS as an analytical function of α, see Eq. (16). We observed no significant differences in the results when using Eq. (16) to represent the EOS for any α.

3.2 Results with DBHF-Based EOS

The energy per particle obtained from Eq. (19) are shown in Table 1 for some magic or semimagic nuclei. We have considered ^{40}Ca as a nucleus with N=Z, two cases with different levels of asymmetry, ^{90}Zr and ^{208}Pb (average asymmetry parameter, $(N - Z)/A$, equal to 0.11 and 0.21, respectively), and a more strongly asymmetric one, ^{266}Pb, for which no experimental information is available, but which could be doubly magic [16]. The binding energy per particle for this nucleus predicted with a phenomenological Skyrme interaction is 6.699 MeV [16].

We have used three relativistic one-boson-exchange potentials, the Bonn A, B, and C potentials. In all cases, the EOS to be used in Eq. (19) is obtained in a DBHF calculation of infinite nuclear matter as described in Section 2.

As is well known, Bonn A is the most attractive among the three potentials [11]. This behaviour is related to the strength of the tensor force, which contributes to nuclear matter binding through second-order contributions to the central force. As a consequence of that, a weaker tensor force implies a larger central force and thus larger binding. In all cases (where experimental information is available), the Bonn B predictions appear to be best, with the significant model dependence reflecting the different saturation energies predicted by the three potentials. This is apparent in Figure 6, where the EOS as a function of the average Fermi momentum is displayed for the three potentials at two representative values of α. The purpose of the figure is to show how the differences among the three curves decrease as the proton fraction decreases, and become very small in the limit of neutron matter. This is because, as we pointed out above, the tensor force is the major source of model dependence among these potentials. The tensor force is mostly reflected in the $^3S_1$ partial wave, which, as a T=0 contribution, will lose strength when the system approaches neutron matter.

In order to compare with the experimental charge radii (also displayed in Table 1),our predicted point proton density is folded with the proton charge form factor to yield the charge density through the usual convolution integral,

$$\rho_{ch}(r) = \int d^3r' g(\vec{r} - \vec{r'})\rho_p(r'), \tag{21}$$

where g is the proton charge form factor which is taken to be of Gaussian shape

Table 1. Binding energy/particle (in MeV) and charge radius (in fm) obtained with three relativistic potentials. Experimental values are also shown.

Nucleus	$b.e.(exp.)$	$r_{ch}(exp.)$	Potential	$b.e.(predicted)$	$r_{ch}(predicted)$
			Bonn A	9.23	3.43
^{40}Ca	8.55	3.48	Bonn B	8.44	3.54
			Bonn C	7.99	3.61
			Bonn A	9.70	4.15
^{90}Zr	8.71	4.27	Bonn B	8.74	4.30
			Bonn C	8.18	4.42
			Bonn A	8.97	5.28
^{208}Pb	7.87	5.50	Bonn B	7.95	5.47
			Bonn C	7.35	5.64
			Bonn A	7.81	5.62
^{266}Pb			Bonn B	6.92	5.84
			Bonn C	6.41	6.02

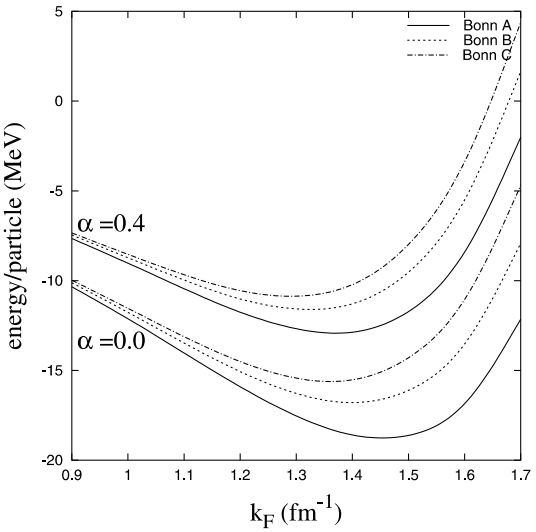

Figure 6. Energy/nucleon as a function of the Fermi momentum predicted with Bonn A (solid line), Bonn B (dotted line), and Bonn C (dash-dot), for α=0 (lower group) and α=0.4 (upper group).

[17],

$$g(r) = (a\sqrt{\pi})^{-3} e^{-r^2/a^2}, \tag{22}$$

and the constant a is related to the charge radius of the proton (equal to 0.8 fm) through $r_{ch,p} = \sqrt{\frac{2}{3}}a$.

As observed with the energies, the best agreement with the charge radii is obtained with Bonn B. The predicted radii getting larger from Bonn A to Bonn C is again a reflection of the larger attraction generated by the former.

Concerning neutron radii and skins, the empirical information available on them is unavoidably indirect, analyses being usually based on fits to proton scattering data. For ^{208}Pb, for instance, analyses of scattering data provide values of the neutron r.m.s. radius ranging from about 5.6 fm to 5.7 fm. The generally accepted range for the neutron skin is quoted as 0.16 $\pm$0.02 fm, but values as large as 0.38 fm have been reported [2]. Most recently, B. Clark and collaborators [3] have found the neutron r.m.s. radius to be between 5.52 and 5.55 fm, and the neutron skin between 0.083 and 0.111 fm. Although in reasonable agreement with non-relativistic Skyrme Hartree-Fock models, these are smaller than the generally accepted values we quoted above, including those from the present study, which are 5.60 fm for the neutron radius and 0.188 fm for the skin (with Bonn B), see Table 2.

In Table 2 we focus on Bonn B predictions for neutron radii and skins. The

Table 2. Neutron radii and neutron skins (in fm) predicted with Bonn B compared with some results from recent analyses. See text for details.

Nucleus	Observable	Bonn B	Other sources
^{40}Ca	r_n	3.40	(3.310,3.314)[b]
	S_n	-0.0454	(-0.067,-0.063)[b]
^{90}Zr	r_n	4.31	
	S_n	0.0809	
^{208}Pb	r_n	5.60	(5.522,5.550),[b] (5.61,5.83)[c]
	S_n	0.188	(0.083,0.111),[b] (0.16,0.38)[c]
^{266}Pb	r_n	6.30	
	S_n	0.518	

[b] Ref [2].
[c] Ref [3].

skin is calculated as the difference between the *point* neutron and proton radii. For comparison, results from recent analyses are also shown. The first entry in the last column refers to the analysis of Ref. [3], while the second entry gives the smallest and largest values from the analysis of Ref. [2]. Clearly, agreement (between analyses and theoretical predictions as well as among various analyses) is still elusive.

Some experimental information specifically on neutron skins is also available for a few isotopic chains, but carries large uncertainties. In Figure 7, our

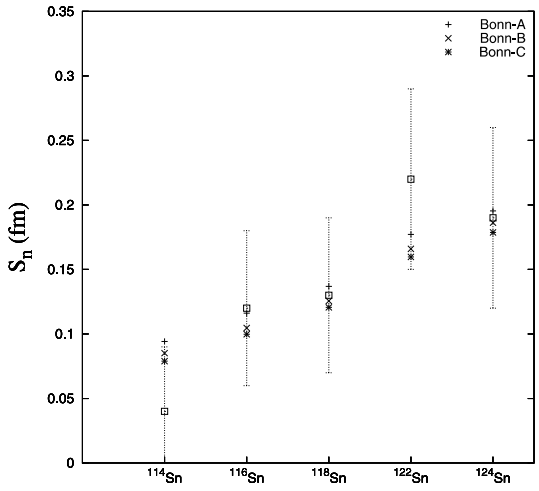

Figure 7. Neutron skins predicted with Bonn A (+), Bonn B ($\times$), and Bonn C ($*$) for Sn isotopes. Data from Ref. [20].

predictions for neutron skins of Sn isotopes are compared with the data of Krasznahorkay *et al.* [18]. The data were obtained from cross section measurements of isovector spin-dipole resonances excited by the (^{3}He,t) charge-exchange reaction at 450 MeV, and are not free of model assumptions [18]. Accurate determinations of neutron skins are obviously needed to discriminate among models.

4 Summary and Conclusions

We have presented calculations of the nuclear matter equation of state when protons and neutrons have different Fermi momenta. The calculations are self-consistent and parameter-free, in the sense that no parameter of the NN force is adjusted in the medium.

We also discussed predictions for nuclear energies, densities, and r.m.s. radii for some nuclei, ranging from symmetric to highly asymmetric. *The nuclei under consideration were chosen so as to sample different levels of asymmetries.* We used a mass formula as a simple yet direct tool to probe our EOS for infinite asymmetric matter in finite nuclei.

We compare with empirical information, when available. Realistic predictions for proton r.m.s. radii and binding energies are obtained if the EOS originates from DBHF calculations. (An alternative popular approach is the use of a nonrelativistic framework together with phenomenological three-body forces.)

Concerning the baseline force, the predictions obtained with Bonn B are definitely best, reflecting a better balance of attraction and repulsion as compared to both Bonn A and C.

The purpose of this part of the paper was not to achieve the most accurate reproduction of empirical radii and energies, but rather to demonstrate that a microscopic density-dependent interaction based on realistic two-body forces and obtained within a DBHF description of asymmetric matter is capable of generating realistic predictions for both energies and radii without phenomenological adjustments, even if used in the simplest framework of a liquid drop model.

Our predictions for neutron radii and neutron skins are consistent with generally accepted values, which, on the other hand, are accompanied by large uncertainties. Additional theoretical work is clearly needed as well as accurate determinations of neutron densities. These may be available in the near future through parity violating measurements of neutron densities which have been proposed as a tool for measuring neutron distributions with unprecedented accuracy [19]. Parity violation arises from the interference of electromagnetic and weak amplitudes, with the Z^0 coupling mainly to neutrons at low Q^2. The data may be interpreted with as much confidence as electromagnetic scattering [19] and should provide more stringent constraints for theoretical models.

Our future plans include microsopic reaction studies with highly asymmetric nuclei using an α- and isospin-dependent effective interaction as discussed

in Ref. [7]. Thus, following the asymmetry profile of a nucleus with the appropriate interaction amounts to selecting the proper balance of T=1 and T=0 contributions, as determined by the relative proton/neutron densities. For instance, the interaction of, say, an incoming neutron near the skin would be predominantly nn, and thus mostly T=1. This "isospin selection" could be important, especially for the more exotic topologies.

Acknowledgments

This work was done in collaboration with D. Alonso (University of Idaho). Financial support from the U.S. Department of Energy under grant No. DE-FG03-00ER41148 is gratefully acknowledged.

References

[1] C.J. Horowitz and J. Piekarewicz (2001) *Phys. Rev. C* **64** 062802.

[2] S. Karataglidis, K. Amos, B.A. Brown, and P.K. Deb (2002) *Phys. Rev. C* **65** 044306.

[3] B.C. Clark, L.J. Kerr, and S. Hama *nucl-th/0209052*.

[4] R.J. Furnstahl (2002) *Nucl. Phys. A* **709** 85.

[5] K. Oyamatsu, I. Tanihata, Y. Sugahara, K. Sumiyoshi, and H. Toki (1998) *Nucl. Phys. A* **634** 3.

[6] T. Suzuki *et al.* (1995) *Phys. Rev. Lett.* **75** 3241.

[7] D. Alonso and F. Sammarruca (2003) *Phys. Rev. C* **67** 054301.

[8] P. Danielewicz, R. Lacey, and W.G. Lynch, www.sciencexpress.org/31 October 2002/ Page 1/10.1126/science.1078070.

[9] M.I. Haftel and F. Tabakin (1970) *Nucl. Phys. A* **158** 1.

[10] R. Brockmann and R. Machleidt (1984) *Phys. Lett.* **149B** 283; (1990) *Phys. Rev. C* **42** 1965.

[11] R. Machleidt (1989) *Adv. Nucl. Phys.* **19** 189.

[12] P. Danielewicz *preprint nucl-th/0203002*.

[13] Bao-An Li (2001) *Nucl. Phys. A* **681** 434c; *nucl-th/0301039*.

[14] M. Prakash, T.L. Ainsworth and J.M. Lattimer (1988) *Phys. Rev. Lett.* **61** 2518.

[15] K. Oyamatsu (1993) *Nucl. Phys. A* **561** 431.

[16] B.A. Brown (1998) *Phys. Rev. C* **58** 220.

[17] D. Vautherin and D.M. Brink (1972) *Phys. Rev. C* **5** 626.

[18] A. Krasznahorkay *et al.* (1999) *Phys. Rev. Lett.* **82** 3216.

[19] C.J. Horowitz, S.J. Pollock, P.A. Souder, and R. Michaels (2001) *Phys. Rev. C* **63** 025501.